Solar Energy 237 (2022) 333–339

Contents lists available at ScienceDirect

Solar Energy

journal homepage: www.elsevier.com/locate/solener

Ab initio study on electronic and optical properties of Cu_2NiGeS_4 for photovoltaic applications

J. El Hamdaoui [a,b], M. El-Yadri [a], K. Lakaal [a,b], M. Kria [a,b], M. Courel [c], M. Ojeda [c], L.M. Pérez [d,*], D. Laroze [e], E. Feddi [a,f,*]

[a] Group of Optoelectronic of Semiconductors and Nanomaterials, ENSAM, Mohammed V University in Rabat, Morocco
[b] Laboratory of Condensed Matter and Interdisciplinary Sciences (LaMCScI), Faculty of Sciences Rabat, Mohammed V University in Rabat, Morocco
[c] Centro Universitario de los Valles, Universidad de Guadalajara, Carretera Guadalajara-Ameca, 46600, Ameca, Jalisco, Mexico
[d] Departamento de Física, FACI, Universidad de Tarapacá, Casilla 7D, Arica, Chile
[e] Instituto de Alta Investigación, CEDENNA, Universidad de Tarapacá, Casilla 7D, Arica, Chile
[f] Institute of Applied Physics, Mohammed VI Polytechnic University, Lot 660, Hay Moulay Rachid Ben Guerir, 43150, Morocco

ARTICLE INFO

Keywords:
Kesterite
CNGS
Electronic properties
Optical properties
Solar cell

ABSTRACT

In this paper, first principle calculations of Cu_2NiGeS_4 (CNGS) are carried out to explore the structural, electronic and optical properties of kesterite compound. Both mBJ+U and HSE potentials are used to calculate the band gap energy. The first approach gives a value of 1.78 eV and the second one a value of 1.76 eV. Our numerical simulation shows that the CNGS exhibits a remarkable high absorption coefficient of the order of 10^4 cm^{-1}, leading to a promising absorber material for photovoltaic devices. Additional optical properties such as refraction index and dielectric function are also calculated in this work. Furthermore, CNGS-based solar cell simulation was performed through SCAPS software. The calculated values of short-circuit current density J_{sc}, open-circuit voltage V_{oc}, Fill factor FF and power conversion efficiency show that CNGS can be a potential candidate for solar cell application.

1. Introduction

Nowadays, one of the most important topics investigated by the scientific community is the generation of electrical energy through sources that are clean, safe, sustainable, renewable, and friendly to the environment (Razmjoo et al., 2021; Panwar et al., 2011). Due to this, a lot of theoretical and experimental research have been performed to understand and improve the process involved in the generation of electricity from the sunlight. As we know, the conversion efficiency from sunlight to electrical energy depends on the photovoltaic device that absorbs the radiation of the sunlight and converts it into electricity (Panwar et al., 2011; Beraich et al., 2020; Gloeckler and Sites, 2005).

Currently, photovoltaic materials such as amorphous silicon, CdTe, and chalcopyrite thin films have received a lot of interest because of their excellent optical properties and high PV efficiency (Ranjan et al., 2021; Ranjan and Chakraborty, 2021; Pham et al., 2021; Eid et al., 2015; Petrović et al., 2015; Ji et al., 2020). However, the majority of these materials contain low-abundance and/or toxic elements, restricting their use on a commercial basis. In particular, some studies have been performed in $Cu_2ZnSnSe_4$ (CZTSe), Cu_2ZnSnS_4 (CZTS) and $Cu_2ZnSn(S_xSe_{1-x})_4$ compounds, which are an alternative for CIGS and CdTe. These three compounds present a kesterite symmetry and have been attracting attention because these materials are earth-abundant and nontoxic. However, the highest reported conversion efficiency is 12.6% even though the band gap is in the range from 1 to 1.5 eV (CZTSSe) with an absorption coefficient higher than 10^4 cm^{-1} (Dattatray and Abhishek, 2019; Delgado and Sagredo, 2020; Padhy et al., 2021; Kim et al., 2016). Therefore, its performance is still far from the 20.8% achieved for CIGSe thin film solar cells (Eid et al., 2015). The main drawbacks in the power conversion performance of kesterite-based thin film solar cell are the presence of secondary phases such as ZnS, SnS, SnS_2, and Cu_2S, the presence of uncontrollable disorder, and the presence of large Cu_{Zn} and Zn_{Cu} antisite defects, leading to potential fluctuations in the electronic band structure and the band tailing (Just et al., 2016; Mangelis et al., 2019; Vanalakar et al., 2018). One of the fascinating approaches to lessen these effects is to replace Cu^+, Zn^{2+}, and Sn^{4+} with other chemical components of the same valence. The substitution of tin (Sn) atoms with germanium (Ge) atoms can increase the optical band gap, allowing it to be coupled with a low band-gap cell in a tandem configuration that can convert a significant part of

* Corresponding authors.
E-mail addresses: lperez@uta.cl (L.M. Pérez), e.Feddi@um5s.net.ma (E. Feddi).

https://doi.org/10.1016/j.solener.2022.03.052
Received 24 January 2022; Received in revised form 18 March 2022; Accepted 19 March 2022
Available online 13 April 2022

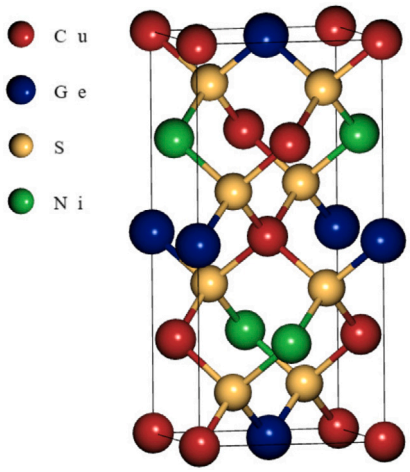

Fig. 1. Schematic representation of Cu_2NiGeS_4 in kesterite structure.

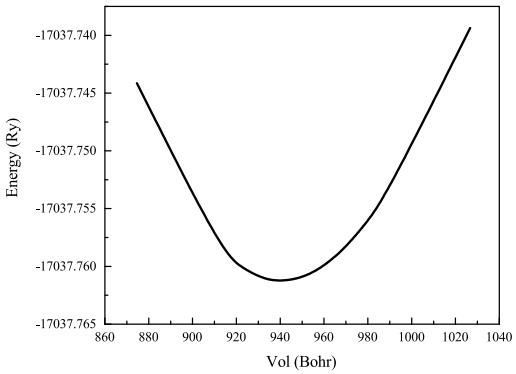

Fig. 2. Total energy as a function of volume of CNGS in kesterite structure.

sunlight into electrical energy while suppressing all Sn-related deep defects. The quaternary chalcogenide semiconductors Cu_2ZnGeX_4 (X = S, Se), defined as CZGX (X = S or Se), have an adjustable band gap between 1.3 and 2 eV (El Hamdaoui et al., 2021).

On the other hand, the substitution of Zn by Ni in the CZGS results in the obtention of Cu_2NiGeS_4 (CNGS) compound, which is also an interesting material for solar cell fabrication. Experimentally, only two works have investigated these materials. Delgado and Sagredo (2020) and Beraich et al. (2020) have successfully synthesized CNGS powder and thin film respectively. They have found that due to the distribution of cations in the tetrahedral sites of these compounds, the CNGS powders present the stannite structure while the kesterite structure is observed in thin films. In addition, they demonstrated that CNGS in kesterite and stannite form can be synthesized with a simple and low-cost spray ultrasonic method. Their samples demonstrate a very high crystallinity and the obtained Kesterite thin films are homogeneous with a band gap of 1.8 eV and with a high absorption coefficient (Beraich et al., 2020). Unfortunately, even though CNGS has some promising properties to make it suitable for solar cells, the research about it is in an embryonic state. At the best of our knowledge, so far there is no theoretical study about the electronic and optical properties of Cu_2NiGeS_4, which could be very useful for the experimental research on this material. In addition, there are no theoretical reports of the CNGS solar cell performance. The solar cell simulation would allow evaluating the potential application of CNGS material to solar cells. In this sense, Density Functional Theory calculations are performed in this work to evaluate the electronic and optical properties of CNGS. In addition, the application of this material to solar cells is analyzed by numerical simulations using SCAPS software.

2. Calculations detail

The standard DFT approach (LDA and GGA) is well known for significantly underestimating bandgap energy (Perdew, 2009). There are several approaches to compensate the bandgap underestimation of standard DFT. In this work we used two of these approaches which are DFT+U (mBJ+U) and hybrid functionals, both methods are commonly employed in theoretical research (Shokri et al., 2020). While DFT+U approach is computationally equivalent to the standard DFT method, the hybrid functionals are computationally costly and more accurate than DFT+U. For DFT+U method we used Tran–Blaha modified Becke and Johnson potential combined (Tran and Blaha, 2009) with the Hubbard potential U (Kirchner-Hall et al., 2021), that is based on the full-potential linearized augmented plane-wave (FP-LAPW) (Blaha et al., 2018) method implemented in wien2k code (Schwarz et al., 2002). mBJ is a correction used for GGA bandgap, however in our case it is not sufficient to obtain a bandgap near the experimental data. Therefore, we associate it with the Hubbard potential which is a semiempirical value that can be added to DFT calculations for any open shell orbitals such as d or f orbitals for transition metals (Cu and Ni in our case) and perovskites when there is a strong correlation (Kirchner-Hall et al., 2021). The band gap value can be altered by adjusting the U value, and in our calculation, several U values were examined. The optimal Hubbard U value that agrees well with experimental data is determined to be 6 eV. For the hybrid functional we used the Heyd–Scuseria–Ernzerhof (HSE) performed with QUANTUM ESPRESSO code (Giannozzi et al., 2009), based on the plane wave (PW) method. In the HSE hybrid functionals, the exchange part of the exchange and correlation potential is a hybridization between the exact Hartree Fock exchange and the exchange of the PBE functional (Heyd et al., 2003):

$$E_{xc}^{HSE} = E_{xc}^{PBE} + \alpha\left(E_x^{sr,HF} - E_x^{sr,PBE}\right) \quad (1)$$

where E_{xc}^{PBE} is the exchange and correlation energy functional of the generalized gradient approximation (GGA-PBE), and $E_x^{sr,PBE}$ and $E_x^{sr,HF}$ are the short-range (sr) part of the PBE exchange and Hartree Fock energies, respectively. The mixing parameter α is chosen to be 0.25 in the original HSE functional. Following the convergence test, within FP-LAPW method, we have taken the muffin-tin radii sufficiently large to avoid their overlapping. The product of the smallest muffin-tin radius and the magnitude of the largest k-vector is set to $R_{mt} * K_{max} = 9$. Cut-off energy of the plane-wave expansion is taken by default to −6 Ry and the number of K-points in the first Brillouin zone is fixed at 1000. For PW calculation, the cut-off energy for the wave function is set to 80 Ry. k-point grid in the Brillouin zone is introduced with a 6 × 6 × 3 grid in the Monkhorst–Pack method (Monkhorst and Pack, 1976).

The relaxed lattice parameters of CNGS are obtained with two methods. The first method via Wien2k package, where the optimized lattice parameters are calculated by fitting the total energy as a function of the volume of the unit cell using Murnaghan's equation of state (Tyuterev and Vast, 2006), and the second method via quantum espresso package, where the lattice parameters are relaxed using Broyden Fletcher Goldfarb Shanno (BFGS) method (Liu and Nocedal, 1989)

To calculate the optical properties, the following dielectric function formula $\varepsilon(\omega) = \varepsilon_r(\omega) + i\varepsilon_i(\omega)$ was used, where ε_r stands for its real part obtained using the Kramers–Kronig transformation (Bikerouin et al., 2020) and ε_i denotes its imaginary part that can be given by the momentum matrix element between the occupied and unoccupied states according to the following equation.

$$\epsilon_i(\omega) = \frac{e^2\hbar}{\pi m^2\omega}\sum_{v,c}\int_{BZ}|\langle cke\nabla\rangle vk|^2\delta(\omega_{ck}(k)-\omega)d^3k \quad (2)$$

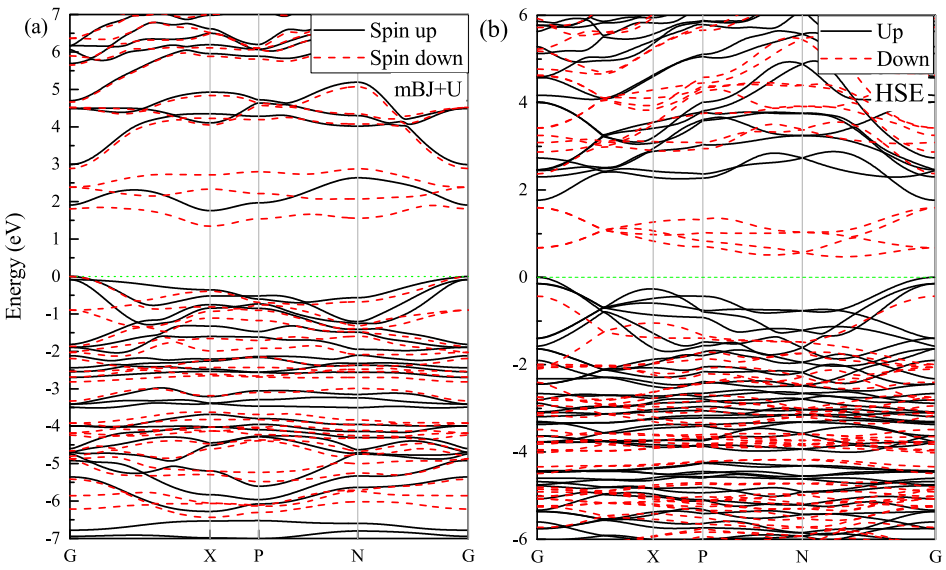

Fig. 3. CNGS band structure with (**a**) mBJ+U and (**b**) HSE06.

Where c and v are the conduction and valence of Kohn–Sham states, respectively.

$$\epsilon_r(\omega) = 1 + 2/\pi \int_0^{\infty} \frac{\epsilon_i(\omega')}{\omega'^2 - \omega^2} \omega' d\omega' \tag{3}$$

3. Results and discussions

3.1. Structural properties

The quaternary Cu_2NiGeS_4 can be crystallized in kesterite structure (Beraich et al., 2020). Fig. 1 presents the sites of each atom in the unit cell structure of CNGS, which is characterized by a pseudo-cubic cell. The atomic position of Cu is 2a (0, 0, 0) and 2c (0, 0.5, 0.25), Ni at 2d (0.5, 0, 0.25), Ge and S are located at 2b (0.5, 0.5, 0) and 8 g (0.7581, 0.2536, 0.8718) respectively, in the tetragonal unit cell with space group I4 (162) (Hall et al., 1978). Fig. 2 presents the fitted data of total energy to unit cell volume obtained with wien2k. Thus, the calculated lattice parameters are a = 5.14 Å, c = 10.5 Å and a = 5.2 Å, c = 10.48 Å with FP-LAPW and PW respectively. We noted that the calculated lattice parameters are in good agreement with the experimental result, where the lattice parameters obtained experimentally by Beraich et al. are a = 5.25 Å and c = 10.7 Å (Beraich et al., 2020).

The Cohesive energy is an important parameter to assess the stability of CNGS in kesterite structure, it is defined as the energy required to decompose the crystal into single atoms. Hence, the more negative the cohesive energy value, the more stable the crystal structure is (Wang et al., 2009). The cohesive energy can be calculated with the following expression:

$$E_C = \left[E_{CNGS} - 2 \times E_{Cu} - E_{Ni} - E_{Ge} - 4 \times E_S\right] \times \frac{1}{8} \tag{4}$$

Where E_{CNGS} is the total energy of CNGS in kesterite structure and E_{Cu}, E_{Ni}, E_{Ge} and E_S are the energies of the isolated atoms in the freedom states. The calculated cohesive energy of kesterite CNGS is 4.34 eV/atom, where E_c is negative, which indicates the stability of our material. Compared with the results known for CZTS material, our calculation shows that CNGS is more stable than CZTS with 3.9 eV/atom (Rondiya et al., 2020)

3.2. Electronic properties

In order to explore the Cu_2NiGeS_4 properties, we should understand the behavior of its electrons. Taking into account the metallic characteristic of nickel element, the spin-polarized effect is strongly requested in the calculations. This will provide a remarkable difference in the CNGS compound depending on where the spin is oriented either up or down. Fig. 3 illustrates the band structure of CNGS kesterite material with two representative cases of spin (up and down) determined with both mBJ+U and HSE06 approaches , along Γ -> X -> P -> N -> Γ symmetric points in irreducible Brillouin zone with Fermi level at 0 eV. From this figure, we can see the impact of the spin orientation especially on the value of CNGS gap energy. As we can see in Fig. 3a, a band-gap value of about 1.78 eV is obtained for CNGS compound when the spin is up, while it is about 1.34 eV for the spin-down case, from the same figure. The maximum of the valance band is located at the center of Brillouin zone Γ, while the minimum of the conduction band is found in X point, where the conduction band in that latter is slightly below the gamma point, where we deduced that mBJ+U shows an indirect bandgap behavior in both spin case. However, it can be seen in Fig. 3b, with the accurate HSE06 calculations that a direct band gap at Γ valley of the first BZ is obtained with a value of 1.76 eV and 0.91 eV in both spin cases up and down respectively. The band gap energy of the majority spin up remains within the range of gap energies found in the literature until now, which is around 1.6–1.8 eV (Beraich et al., 2020).

To further examine the electronic behavior of CNGS, we have also computed the densities of states to investigate the contribution of CNGS elements in forming its electronic structure. Fig. 4 presents the total and the partial densities of states of the main elements contributing in forming the band structure. For both cases in question, the upper of the valence band is typically composed by the Cu d-orbitals, while the lower of the conduction band in the spin down case is predominantly formed by the electrons of d-orbital of Ni, the spin up case is a hybridization between the s and p orbital of Ge and S. The top of the conduction band is manly formed from the p-orbitals of Ge in the spin up case, in contrast with the spin down, which is a mixing between p and d-orbitals of Ge and Ni respectively. On the other hand, the bottom of the valence band is a hybridization of d-orbitals of Ge and Ni with p-orbital of S. The obtained band gap energy of CNGS is lower than the quaternary kesterite CZGS which has bandgap between 2–2.2 eV according to numerous studies (El Hamdaoui et al., 2021). The substitution of the Zn atoms by Ni serves primarily to reduce the band

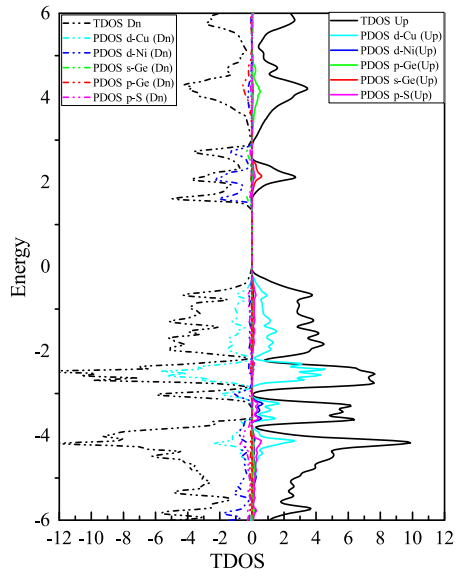

Fig. 4. The total density of states of CNGS and the partial one of particular orbitals which have a strong contribution in both spin states.

Table 1
The calculated total and partial magnetic moment.

	Total	Cu	Ni	Ge	S
μ (μ_B)	2	0.03	1.655	0.001	0.034

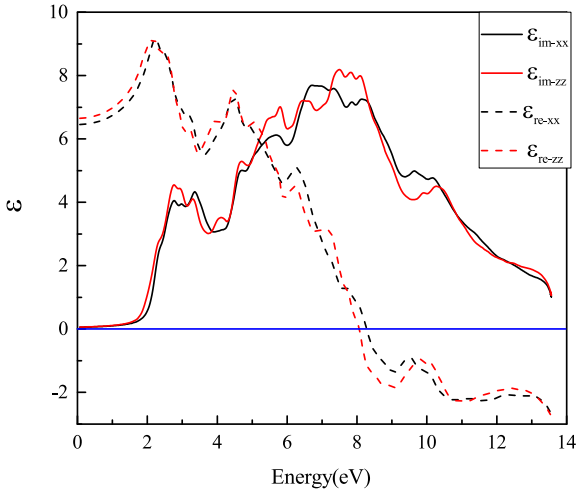

Fig. 5. The imaginary and real parts of dielectric function spectra of CNGS.

gap from 2.2 to 1.8 eV. These results indicate that a band gap between 1.2 and 1.4 is expected if we substitute the sulfur with selenium.

The presence of Ni atoms can induce a magnetic behavior in the kesterite compound. This can be observed in the difference in total dos in both spin states. However, the magnetic origin can be evaluated by magnetic moment. Hence, the calculated total and partial magnetic moment are presented in Table 1. The computed total magnetic moment is found to be 2 while the partial magnetic moment of Ni is 1.65 and the other atoms present a weak magnetic moment. This shows that the origin of magnetization in quaternary CNGS is the Ni atom.

3.3. Optical properties

To provide a clear picture of the impact of Ni incorporation into kesterite structure, we determine with mBJ+U the optical properties of CNGS from which we calculate the optoelectronic parameters of solar cells. As usual, this can get started with the investigation of the dielectric function. The calculated imaginary part ε_{im} and real part ε_{re} of the dielectric function of CNGS are shown in Fig. 5 with two possible directions of polarization. It is obvious that at low energies, the curves of the imaginary in-plane and out-of-plane components ε_{im-xx} and ε_{im-zz} respectively are almost similar, hence the imaginary dielectric function is isotrope. Above the first critical photon energy, which is close to band gap energy, the spectra of ε_{im} present the first peaks at the visible range corresponding either to direct or indirect interband transitions from the highest valence band (from d-state of Cu) to the lowest conduction band (to s-state of Ge). On the other hand, the calculated longitudinal and transversal components of the real part of the dielectric function provide informations on the value of the static dielectric constant, which corresponds to the limit value at zero frequency. We have found that $\varepsilon_{re-xx} = 6.65$ and $\varepsilon_{re-zz} = 6.45$, two values from which we calculated the average value that can be used as one of the essential parameter to predict the performance of solar cells based on CNGS kesterite. Furthermore, CNGS reaches a negative values of ε_{re} over the range of UV. Consequently, the CNGS kesterite can be an appealing material for UV-plasmonics. As it is known, the measurements of the imaginary part of dielectric function allow to deduce the optical absorption coefficient, which also allows us to specify the region of the electromagnetic waves spectrum that the CNGS kesterite can be exposed as a potential absorber. Fig. 6a depicts the in-plane and out-of-plane components of absorption coefficient. As it can be seen, the absorption process occurs with the energy range greater than or equal the CNGS gap energy and has an order of magnitude of 10^4 cm^{-1} in the visible range.

Other required parameters used to predict the behavior of optoelectronic devices such as solar cells are the refractive index and extinction coefficient, which describe the loss of photon energy during propagation through the optical medium. These can be deduced from ε_{re} and ε_{im} as follows (El Hamdaoui et al., 2021):

$$n(\omega) = \frac{1}{2}[(\varepsilon_{re}^2(\omega) + \varepsilon_{im}^2(\omega))^{1/2} + \varepsilon_{re}(\omega)]^{1/2} \quad (5)$$

$$k(\omega) = \frac{1}{2}[(\varepsilon_{re}^2(\omega) + \varepsilon_{im}^2(\omega))^{1/2} - \varepsilon_{re}(\omega)]^{1/2} \quad (6)$$

In Fig. 7, both parallel and perpendicular components of refractive index and extinction coefficient of CNGS kesterite are illustrated as functions of the incident photon energy. It is remarkable that $n(w)$ and $k(w)$ behave like ε_{re} and ε_{im} respectively. They also present their first peaks at the same threshold energy. From the measurement point of view, the corresponding values of CNGS static refractive indices are $n_{0-xx} = 2.54$ and $n_{0-zz} = 2.58$, which are slightly greater than those obtained from our previous work on CZGS (El Hamdaoui et al., 2021)

4. Solar cell application

4.1. Device structure and simulation

Following the optical responses of CNGS calculated above, we next proceed to perform the numerical simulations of the photovoltaic solar cell using the material of interest as an absorber layer. Since CNGS is a part of the kesterite family, we consider the traditional configuration of CZTS and CIGS for CNGS baseline (Et-taya et al., 2020; Jackson et al., 2016). The traditional Mo/CNGS/CdS/ ZnO/ZnO:Al configuration is presented in Fig. 8a, where Mo is the back contact, CNGS is the p-type absorber and the other part of the PN junction is the n-type CdS buffer layer. On the top of CdS, an intrinsic layer of ZnO and Al-doped ZnO (ZnO:Al) as a transparent conducting oxide layer (TCO), acting as the window layer are considered.

The simulation is carried out by the SCAPS-1D program, which was developed at the university of Gent, Belgium (Burgelman et al., 2018). SCAPS determines the JV characteristics and spectral response

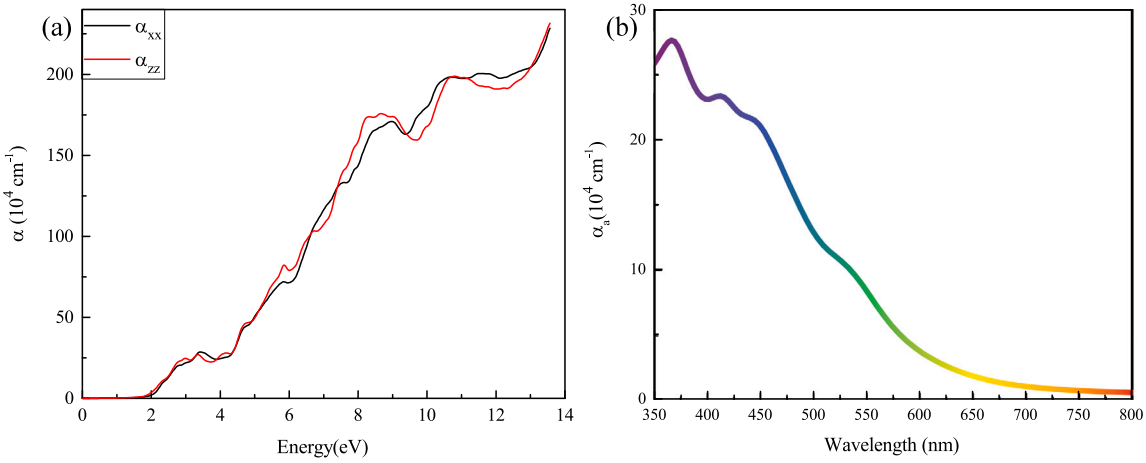

Fig. 6. The CNGS absorption coefficient spectra as functions of the incident photon energy, (a) the in-plane and out-of-plane components, (b) the average absorption coefficient in the visible range.

Table 2
Physical parameters of each layer used in the simulation of CNGS solar cell (Kukreti et al., 2021; Courel et al., 2016; Fujiwara and Collins, 2018; Beal and Hughes, 1979; Luo et al., 2021; Adewoyin et al., 2017).

Parameters	ZnO:Al	ZnO	CdS	CNGS	MoS_2
ω	80	80	50	2000	80
E_g(eV)	3.3	3.3	2.4	1.8[a]	1.3
X (eV)	4.5	4.5	4.4	4.5	4.2
ϵ	9	9	10	6.56[a]	4
n_0	2	2	2.5	2.56[a]	4.77
N_c (cm^{-3})	2.2 10^{18}	2.2 10^{18}	2.2 10^{18}	2.58 10^{18}[a]	7.5 10^{17}
N_v(cm^{-3})	1.810^{19}	1.8 10^{19}	1.8 10^{19}	4.54 10^{18}[a]	1.8 10^{18}
v_e(cm/s)	10^7	10^7	10^7	10^7	10^5
v_h (cm/s)	10^7	10^7	10^7	10^7	10^7
μ_e (cm^{-2}/Vs)	100	100	100	100	100
μ_h (cm^2/Vs)	25	25	25	25	150
N_D (cm^{-3})	10^{18}	10^{18}	10^{18}	0	0
N_A (cm^{-3})	0	0	0	10^{16}	10^{15}
Absorption	Scaps file	Scaps file	Scaps file	Experimental data (Beal and Hughes, 1979)	Data Fig. 6,b
m_e[a](m_0)	0.27	0.27	0.25	0.22[a]	0.53
m_h[a](m_0)	0.59	0.59	0.7	0.32[a]	0.62

[a](Computed in this work.)

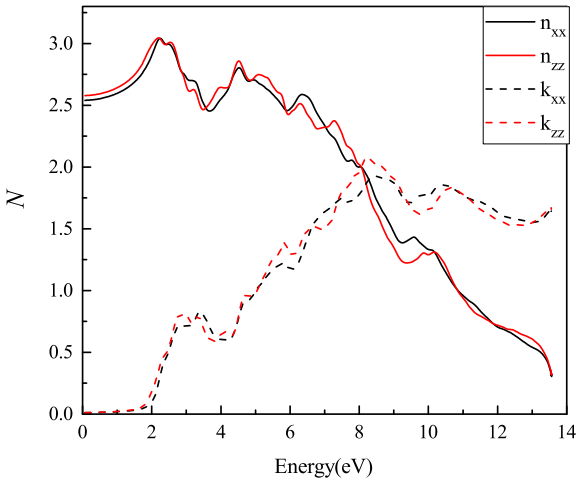

Fig. 7. Variation of the refractive index (solid line) and extinction coefficient (dashed-line) of CNGS kesterite as functions of the incident photon energy. For both quantities the in-plane and out-plane components are calculated.

by solving the basic semiconductor equations such as continuity equation, Poisson equation and carrier transport equation. These equations are treated in one dimension and steady-state condition (Burgelman et al., 2000; Niemegeers and Burgelman, 1997; Minbashi et al., 2018). The simulation with SCAPS requires a set of input parameters of the device and the material of each layer, which were obtained either from different works and experimental literature studies (Kukreti et al., 2021; Courel et al., 2016; Fujiwara and Collins, 2018; Beal and Hughes, 1979; Luo et al., 2021; Adewoyin et al., 2017) or computed with DFT. All the parameters used in the simulation are summarized in Table 2.

In this simulation, the work function of the back contact Mo is taken as 5 eV and the surface recombination velocity as 10^5 cm.s^{-1} and 10^7 cm.s^{-1} for electron and hole respectively (Et-taya et al., 2020). A single defect type is considered in the absorber layer located in the middle of the band gap with a capture cross-section of electron and hole of 10^{-14} cm^2 and a density of 10^{15} cm^{-3} (Li et al., 2019; Chen et al., 2010). In addition, the radiative recombination is considered in our simulation because auger recombination is known to contribute only at high carrier concentrations. Moreover, the radiative recombination of CNGS and the other layer are calculated with the following equation (Jiménez et al., 2018):

$$B = \frac{8.\pi.n_r^2}{c^2.h^3.n_i^2}\int_{E_g}^{\infty}\frac{\alpha(E).E^2.dE}{e^{\frac{E}{Kb.T}}-1} \quad (7)$$

Where n_r is the refractive index of the material, c the speed of light in vacuum, E_g the band gap energy and $\alpha(E)$ the absorption coefficient as

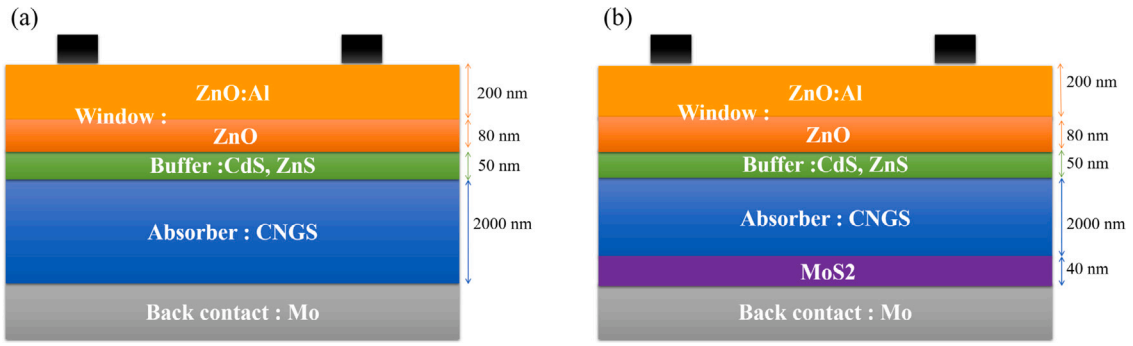

Fig. 8. The schematic representation of CNGS solar cell devices, (a) without MoS_2 and (b) with MoS_2 interlayer.

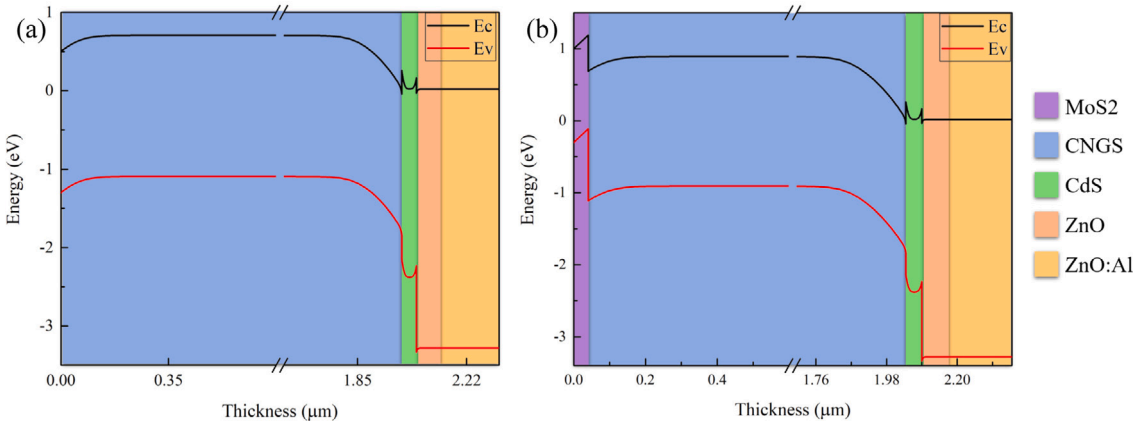

Fig. 9. The energy band diagram of CNGS solar cell devices, (a) without MoS_2 and (b) with MoS_2 interlayer.

a function of wavelength for direct band-gap. The effective density of states of the conduction and valence band can be calculated by:

$$N_c = 2\left(\frac{2.\pi.m_e^*.K_b.T}{h^2}\right)^{3/2} \tag{8}$$

$$N_v = 2\left(\frac{2.\pi.m_h^*.K_b.T}{h^2}\right)^{3/2} \tag{9}$$

Here effective masses are obtained using the parabolic band approximation by parabolic fitting the band edge with the following equation (Farkousa et al., 2021)

$$m^* = \hbar\left(\frac{\partial^2 E_b}{\partial k^2}\right)^{-1} \tag{10}$$

Where m_e^* and m_h^* are the effective mass of electron and hole respectively, E_b and k denoted the energy of the band of interest and k is the wave vector. The absorption coefficient data of each layer was imported from an external source, for CNGS we use the Data of Fig. 6b, and the other layers are taken from the experimental results in the literature (Fujiwara and Collins, 2018; Beal and Hughes, 1979). In this work, we have considered the experimental series and shunt resistances of CZTS as 4.5 $\Omega \cdot cm^2$ and 340 $\Omega \cdot cm^2$, respectively (Karthick et al., 2020). The cell was illuminated from the TCO side with AM1.5G spectrum.

4.2. Simulations results

4.2.1. Energy band diagram

The energy band diagram provides an insight into the band alignment that impacts the photogenerated carrier transport, carrier recombination across the heterojunction and thus influences the solar cell performance. Fig. 9a shows the band diagram of the CNGS baseline cell. The most important part of the band diagram is at the interface between the absorber (CNGS) and the buffer (CdS) layers, where a so-called spike-like shape is observed. It is well known that the spike form interface is favorable for high efficiency (Haddout et al., 2019). Indeed, it enhances the collection of the photo-generated electrons as a result of the reduction of recombination rate at the interface, which leads to higher V_{oc}, and thereby raising the solar cell performance.

4.2.2. CNGS baseline characteristics

The current–voltage plot of CNGS baseline is shown in Fig. 10 (black line), which allows us to extract the indispensable solar cell characteristics. CNGS baseline cell exhibits an efficiency of 6.25%, a fill factor of 49.17% and the other parameters are 0.44 V and 28.635 mA/cm^2 in V_{oc} and J_{sc} respectively. According to Shockley–Queisser limit (Shockley and Queisser, 1961), CNGS with a band gap of 1.8 eV should have at least a PCE of 25%. However, the 6.25% PCE still lags significantly behind the theoretical efficiency. Therefore, to enhance the performance of the CNGS baseline, we add a thin layer of MoS_2 as an interlayer between CNGS and molybdenum. Fig. 8b presents the CNGS solar cell device with MoS_2. It has been reported that the p-type MoS_2 has a positive effect on efficiency improvement (Luo et al., 2021).

4.2.3. Enhancing CNGS cell with MoS_2 interlayer

As it can be seen in Fig. 10 (red plot) the addition of the p-MoS_2 layer yields to improve the efficiency from 6.25% to 10.94%, the same thing occurs for V_{oc}, J_{sc}, and FF where the new obtained values are 0.648 V, 29.039 mA/cm^2 and 58.07%. Although there is not much change in J_{sc} between the two simulated devices, there is a significant enhancement in the V_{oc}. Consequently, the fill factor increases leading to a rise of solar cell efficiency. These results can be explained by rectifying contact between MoS_2 and Mo, which reduced the series resistance that causes an increase in the open-circuit voltage. Furthermore, many researchers used the MoS_2 layer to adjust the mismatch between CZTS and Mo (Adewoyin et al., 2017).

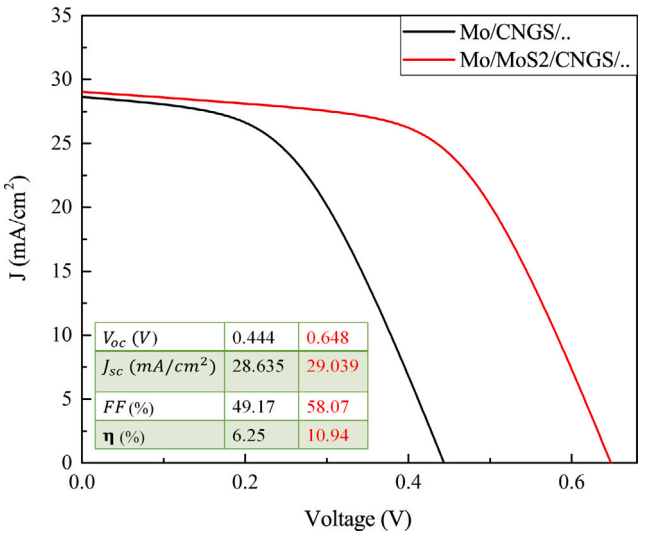

Fig. 10. The current–voltage characteristics of CNGS solar cell devices. (For interpretation of the references to color in this figure legend, the reader is referred to the web version of this article.)

5. Conclusion

In conclusion, we investigated the electronic and optical properties of Cu_2NiGeS_4 in its Kesterite structure. We obtained a band gap energy of 1.78 and 1.76 for mBJ+U and HSE respectively. These results are in good agreement with the reported experimental data. The optical absorption coefficient of CNGS reaches more than 10^4 cm^{-1} in the visible region. Based on this impressive result, we have performed a simulation of CNGS based solar cell taking into consideration the effect of defect and resistances in our model. We found that the solar cell efficiency can reach a value of 10.94%. Pointing out these results, the CNGS kesterite can be considered as a promising absorber material. Further experimental and theoretical studies are needed to achieve a good solar cell efficiency.

Declaration of competing interest

The authors declare that they have no known competing financial interests or personal relationships that could have appeared to influence the work reported in this paper.

Acknowledgments

The authors thank the technical and computational support of M. J. Suazo (UTA, Chile). LMP acknowledges financial support from ANID through Convocatoria Nacional Subvención a Instalación en la Academia Convocatoria Año 2021, Grant SA77210040. DL acknowledges partial financial support from Centers of Excellence with BASAL/ANID financing, AFB180001, CEDENNA.

References

Adewoyin, A.D., Olopade, M.A., Chendo, M.A., 2017. Optik 133, 122–131.
Beal, A.R., Hughes, H.P., 1979. J. Phys. C: Solid State Phys. 12, 881.
Beraich, M., Shailib, H., Benhsinac, E., Hafidid, Z., Taibid, M., et al., 2020. Appl. Surf. Sci. 527, 146800.
Bikerouin, M., Balli, M., Farkous, M., El-Yadri, M., Dujardin, F., Abdellah, A.B., Feddi, E., Correa, J.D., Mora-Ramos, M.E., 2020. Thin Solid Films 696, 137783.
Blaha, P., Schwarz, K., Madsen, G., Kvasnicka, D., Luitz, J., Laskowski, R., Tran, F., Marks, L., 2018. Techn. Universität Wien, Austria.
Burgelman, M., Nollet, P., Degrave, S., 2000. 361(45), 527–532.
Burgelman, M., et al., 2018. SCAPS Manual. University of Gent, Belgium.
Chen, h., Yang, J., Gong, X.G., Walsh, A., Wei, S., 2010. Phys. Rev. B 81, 245204.
Courel, M., Andrade-Arvizu, J.A., Vigil-Galán, O., 2016. Mater. Res. Express 3, 095501.
Dattatray, S.Dhawale, Abhishek, C.Ali.Adnan.Lokhande, 2019. Sustain. Energy Fuels 6, 1365–1383.
Delgado, G.E., Sagredo, V., 2020. Rev. Mex. Fis. 65, 510.
Eid, Jessica, Liang, Haifan, Gereige, Issam, Lee, Sang, Duren, Jeroen Van, 2015. Prog. Photovolt. 23, 269–280.
El Hamdaoui, J., El-Yadri, M., Farkous, M., Kria, M., Courel, M., Ojeda, M., Pérez, L.M., Tiutiunnyk, A., Laroze, D., Feddi, E., 2021. Nanomaterials 11, 2692.
Et-taya, L., Ouslimane, T., Benami, A., 2020. Sol. Energy 201, 827–835.
Farkousa, M., El-Yadri, M., Erguig, H., Pérez, L.M., Laroze, D., et al., 2021. Physica E 134, 114826.
Fujiwara, H., Collins, R.W., 2018. Spectrosc. Ellipsom. Photovolt. 2.
Giannozzi, P., Baroni, S., Bonini, N., Calandra, M., Car, R., Cavazzoni, C., Ceresoli, D., Chiarotti, G.L., Cococcioni, M., Dabo, I., et al., 2009. J. Phys.: Condens. Matter 39, 395502.
Gloeckler, M., Sites, J.R., 2005. Thin Solid Films 480–481, 241–245.
Haddout, A., Raidou, A., Fahoume, M., 2019. Appl. Phys. A 125.
Hall, S.R., Symanski, J.T., Stewart, J.M., 1978. Can. Mineral. 16, 131–137.
Heyd, J., Scuseria, G.E., Ernzerhof, M., 2003. J. Chem. Phys. 18, 8207.
Jackson, P., et al., 2016. Phys. Status Solidi (RRL) 10, 583–586.
Ji, Jung-Min, Zhou, Haoran, Eom, Yu Kyung, Kim, Chul Hoon, Kim, Hwan Kyu, 2020. Adv. Energy Mater. 10, 2000124.
Jiménez, T., Seuret-Jimenez, D., Vigil-Galán, O., Basurto-Pensado1, M.A., Courel, M., 2018. J. Phys. D: Appl. Phys..
Just, J., Sutter-Fella, C.M., Lützenkirchen-Hecht, D., Frahm, R., Schorr, S., Unold, T., 2016. Phys. Chem. Chem. Phys. 18, 15988–15994.
Karthick, S., Velumani, S., Boucléc, J., 2020. Sol. Energy 205, 349–357.
Kim, Shinho, Kim, Kang Min, Tampo, Hitoshi, Shibata, Hajime, Niki, Shigeru, 2016. Appl. Phys. Express 9, 102301.
Kirchner-Hall, N.E., Zhao, W., Xiong, Y., Timrov, I., Dabo, I., 2021. Appl. Sci. 11, 2395.
Kukreti, S., Gupta, G.K., Dixit, A., 2021. Sol. Energy 225, 802–813.
Li, J., Yuan, Z., Chen, S., Gong, X., Wei, S., 2019. Chem. Mater. 31, 826–833.
Liu, D.C., Nocedal, J., 1989. Phys. Rev. B 45, 503–528.
Luo, H., Zhang, Y., Li, H., 2021. Sol. Energy 223, 384–394.
Mangelis, P., Aziz, A., Da Silva, I., Grau-Crespo, R., Vaqueiro, P., Powell, A.V., 2019. Phys. Chem. Chem. Phys. 21, 19311–19317.
Minbashi, M., Ghobadi, A., Ehsani, M.H., Rezagholipour Dizaji, H., Memarian, N., 2018. Sol. Energy 176, 520–525.
Monkhorst, H.J., Pack, J.D., 1976. Phys. Rev. B 13, 5188.
Niemegeers, A., Burgelman, M., 1997. J. Appl. Phys. 81, 2881.
Padhy, Srinibasa, Mannu, Rajeshwari, Singh, Udai P., 2021. Sol. Energy 216, 601–609.
Panwar, N.L., Kaushik, S.C., Kothari, Surendra, 2011. Renew. Sustain. Energy Rev. 15, 1513–1524.
Perdew, J.P., 2009. Int. J. Quantum Chem. 28, 497–523.
Petrović, Miloš, Chellappan, Vijila, Ramakrishna, Seeram, 2015. Sol. Energy 122, 678–699.
Pham, Duy Phong, Lee, Sunhwa, Yi, Junsin, 2021. Physica B 611, 412856.
Ranjan, P., Chakraborty, T., 2021. Mater. Sci. Semicond. Process. 127, 105745.
Ranjan, P., Kumar, P., Surolia, P.K., Chakraborty, T., 2021. Thin Solid Films 717, 138469.
Razmjoo, A., Gakenia Kaigutha, L., Vaziri Rad, M.A., Marzband, M., Davarpanah, A., Denai, M., 2021. Renew. Energy 164, 46–57.
Rondiya, S.R., Jadhav, Y., Dzade, N.Y., Ahammed, R., Goswami, T., Sarkar, A.D., Jadkar, S., Haram, S., Ghosh, H.N., 2020. ACS Appl. Energy Mater. 3, 5153–5162.
Schwarz, K., Blaha, P., Madsen, G.K., 2002. Comput. Phys. Comm. 147, 71–76.
Shockley, W., Queisser, H.J., 1961. J. Appl. Phys. 32, 510.
Shokri, A., Yazdani, A., Rahimi, K., 2020. J. Appl. Phys. 22, 51100756.
Tran, F., Blaha, P., 2009. Phys. Rev. Lett. 102, 226401-226405.
Tyuterev, V.G., Vast, N., 2006. Murnaghan's equation of state for the electronic ground state energy. Comput. Mater. Sci. 38, 350–353.
Vanalakar, S.A., Patil, P.S., Kim, J.H., 2018. Sol. Energy Mater. Sol. Cells 182, 204–219.
Wang, X.F., Li, W., Fang, G.P., Wu, C.W., Lin, J.G., 2009. Intermetallics 17, 768–773.